# Achieving Sub-Hz Frequency Symmetry in Micro-Glassblown Wineglass Resonators

Doruk Senkal, *Student Member, IEEE*, Mohammed J. Ahamed, *Member, IEEE*, Alexander A. Trusov, *Member, IEEE*, and Andrei M. Shkel, *Senior Member, IEEE*

***Abstract*— We demonstrate, for the first time, sub-1 Hz frequency symmetry in micro-glassblown wineglass resonators with integrated electrode structures. A new fabrication process based on deep glass dry etching was developed to fabricate micro-wineglasses with self-aligned stem structures and integrated electrodes. The wineglass modes were identified by electrostatic excitation and mapping the velocity of motion along the perimeter using laser Doppler interferometry. A frequency split ($\Delta f$) of 0.15 and 0.2 Hz was demonstrated for $n = 2$ and $n = 3$ wineglass modes, respectively. To verify the repeatability of the results, a total of five devices were tested, three out of five devices showed $\Delta f < 5$ Hz. Frequency split stayed below 1 Hz for dc bias voltages up to 100 V, confirming that the low frequency split is attributed to high structural symmetry and not to capacitive tuning. High structural symmetry (<1 Hz) and atomically smooth surfaces (0.23 nm Sa) of the resonators may enable new classes of high performance 3-D MEMS devices, such as rate-integrating MEMS gyroscopes. [2013-0209]**

***Index Terms*— Micro-glassblowing, wineglass resonator, 3-D MEMS, degenerate wineglass modes, structural symmetry.**

## I. Introduction

MOTIVATED by the proven performance of macro-scale Hemispherical Resonator Gyroscopes (HRG) [1], there has been a growing interest in 3-D MEMS wineglass resonator architectures for use in timing and inertial sensing applications. Wineglass architectures may enable a new class of high performance dynamic MEMS devices due to potential advantages in symmetry, minimization of energy losses and immunity to external vibrations [1].

However, wafer-scale fabrication of smooth, symmetric and high aspect ratio 3-D structures through micro-machining processes remains to be a challenge. For example, rate integrating gyroscope performance relies heavily on the stiffness asymmetry ($\Delta f$) and damping asymmetry ($\Delta \tau$) between the two degenerate modes [2]. For macro-scale rate integrating gyroscopes this frequency symmetry is obtained through a combination of precision machining processes ($10^{-6}$ relative tolerance) and post fabrication trimming of the resonators [1]. Whereas conventional micro-machining processes are generally associated with low relative tolerances ($10^{-2} - 10^{-4}$ relative tolerance) and flat structures. Factors such as mold non-uniformity, alignment errors or high surface roughness and granularity of deposited thin films have so far prevented fabrication of high precision 3-D wineglass structures using MEMS techniques.

Several examples of MEMS wineglass resonators have been reported in the literature. In [3] hemispherical shells were fabricated by thermally growing oxide in isotropically etched cavities lowest as-fabricated frequency split was measured at 94 Hz. In [4] diamond hemispherical shells were also fabricated, using micro-crystalline diamond deposition into hemispherical molds, a frequency split of ~770 Hz was observed at ~35 kHz center frequency. In [5] a similar process based on deposition of silicon nitride thin films and isotropic etching of silicon has also been explored, minimum etch non-uniformity of 1.4 % was observed inside the molds due to the crystalline orientation dependent preferential etching in silicon. This effect may be a contributing factor in frequency asymmetry observed in [3] and [4]. Alternative fabrication techniques include thin film deposition onto high-precision ball bearings [6], blow-molding of bulk metallic glasses [7] and blow-torch molding of fused silica [8]. Q-factors as high ~300.000 were observed on blow-torch molded devices with relative frequency splits ($\Delta f_{n=2}/f_{n=2}$, ratio of frequency split between the two degenerate modes to central frequency) varying between 0.24 % and 4.49 % [8]. A ~2× variation in central frequency was also observed, which was associated with variations in molding duration and the consequent thickness variation.

In this paper, we explore an alternative approach under the hypothesis that surface tension and pressure driven micro-glassblowing paradigm may serve as an enabling mechanism for wafer-scale fabrication of extremely symmetric ($\Delta f < 1$ Hz, $\Delta f_{n=2}/f_{n=2} < 10$ ppm) and atomically smooth (0.23 nm Sa) 3-D wineglass structures. Micro-glassblowing process relies on viscous deformation of the device layer under the influence of surface tension and pressure forces to define the 3-D shell structure as opposed to conventional deposition, molding or etching techniques. During the brief duration while the device layer is still viscous, surface tension forces act on the 3-D shell structure at an atomic level to minimize surface roughness and structural imperfections. Our hypothesis is that this may lead to levels of smoothness and structural symmetry that is not available through conventional fabrication techniques.

Micro-glassblowing of borosilicate glass for fabrication of spherical shell structures has previously been demonstrated by [9]–[11]. The micro-glassblowing process has also been

Manuscript received June 30, 2013; revised September 23, 2013; accepted October 11, 2013. Date of publication November 1, 2013; date of current version January 30, 2014. This work was supported by the Defense Advanced Research Projects Agency under Grant W31P4Q-11-1-0006. Subject Editor S. M. Spearing.

The authors are with the University of California, Irvine, CA 92697 USA (e-mail: dsenkal@uci.edu; mahamed@uci.edu; atrusov@uci.edu; ashkel@uci.edu).

Color versions of one or more of the figures in this paper are available online at http://ieeexplore.ieee.org.

Digital Object Identifier 10.1109/JMEMS.2013.2286820

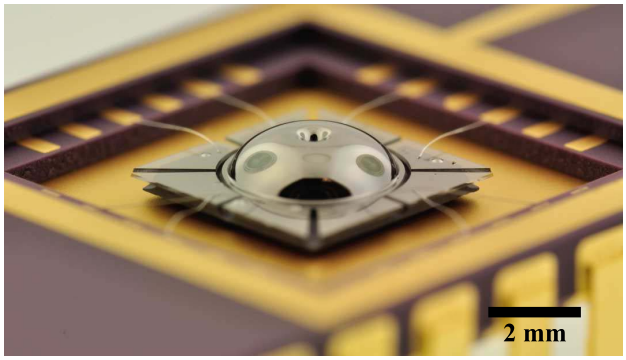


Fig. 1. Packaged and wirebonded micro-wineglass resonator. Diameter 4.4 mm, thickness 50 $\mu$m.

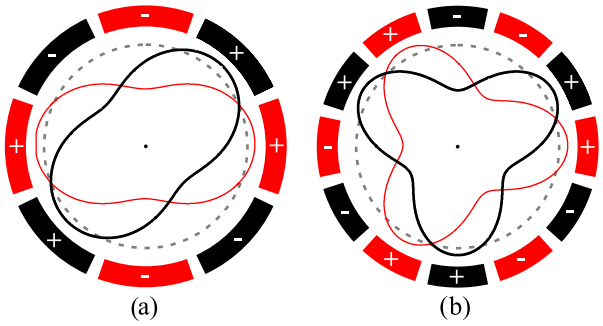


Fig. 2. Mode shapes and minimal electrode configuration required for $n = 2$ (a) and $n = 3$ (b) wineglass modes. (+) and (−) signs denote, in-phase and anti-phase motion.

demonstrated on low internal-loss materials such as Ultra Low Expansion Titania Silica Glass (ULE TSG) and fused silica at temperatures as high as 1700 °C [12], [13]. Characterization methods to identify wineglass modes were later presented in [14] by using assembled electrode structures and mechanical stimuli. Mechanical characterization using the piezo-pinger setup with optical pick-off showed a frequency split of ∼28 Hz on $n = 2$ degenerate wineglass modes [14]. This paper focuses on improvements in fabrication process to incorporate in-situ electrode structures, Fig. 1, [15] as well as further improvement in as-fabricated frequency split, demonstrating $\Delta f < 1$ Hz. This demonstration supports our hypothesis that surface tension and pressure driven micro-glassblowing process results in highly symmetric micro-wineglass structures.

In the following sections, we will first present application of frequency symmetry scaling laws to MEMS wineglass resonators. This will be followed by effect of surface tension forces on micro-glassblown resonators in Section II-A and factors affecting frequency symmetry in Section II-C. In Section III we will present improvements in fabrication process to incorporate in-situ electrode structures to the micro-glassblown resonators as well as further improvement in as-fabricated frequency split. In Section IV we will present the frequency symmetry characterization results from 5 wineglass resonators. The paper concludes with a discussion of the results and $\Delta f$ comparison between multiple micro-glassblown wineglass resonators, Section V.

## II. Design for High Frequency Symmetry

### *A. Frequency Symmetry Scaling Laws in Micro-Scale Hemispherical Resonator Gyroscopes (HRGs)*

Compared to macro-scale HRGs [1], MEMS wineglass resonators have orders of magnitude smaller dimensions, both in shell thickness and diameter. This act of miniaturization requires fabrication processes with very demanding absolute tolerances in order to obtain the required frequency symmetry. In this section, HRG scaling laws are applied to MEMS sized wineglass resonators to demonstrate the effect of miniaturization.

The geometric imperfections of wineglass resonators can be specified using Fourier series representation of the thickness around the central axis of symmetry, Fig. 3 [16]:

$$h(\varphi) = h_0 + \sum_{i=1}^{\infty} h_i \cos i(\phi - \phi_i)\,, \tag{1}$$

where $h(\varphi)$ is the thickness of the wineglass resonator along its perimeter and Eq. 1 is the Fourier series representation of $h(\varphi)$ with respect to azimuth angle $\phi$ such that: $h_0$ is the average thickness and $h_i$ is the $i$th thickness harmonic. This thickness variation will create a corresponding mass variation around the central axis of symmetry of the wineglass resonator according to [16]:

$$M(\varphi) = M_0 + \sum_{i=1}^{\infty} M_i \cos i(\phi - \phi_i)\,, \tag{2}$$

where $M_0$ is the average mass per unit angle and $M_i$ is the $i$th harmonic of the thickness variation.

For gyroscope applications the most commonly used resonance modes are the first two wineglass modes or the so called n = 2 and n = 3 wineglass modes, Fig. 2. This is due to the fact that lower order wineglass modes have higher angular gain factors and lower resonance frequencies. Each wineglass mode has two degenerate modes that are spaced 45° and 30° apart for n = 2 and n = 3 modes respectively. For very low fundamental frequency splits, the degenerate mode pair becomes indistinguishable. Any coriolis input into the resonator causes the mode shape to rotate at an angle proportional to angle of rotation. Rate integrating gyroscopes operate by directly measuring this angle.

It has been shown in [17] and [18] that a fundamental frequency split in these degenerate modes will be observed only if there is a thickness variation on $i = 4$ or $i = 6$ harmonics, respectively (only if i = 2 n). This fact makes the wineglass resonators robust to frequency asymmetries. For example, any imperfection in the 1st, 2nd or 3rd thickness harmonics will have no effect on the frequency symmetry of the n = 2 wineglass mode (see the Appendix).

When the 4th thickness harmonic is not zero, the contribution to the fundamental frequency splitting of n = 2 wineglass mode becomes linearly proportional to the 4th harmonic of the

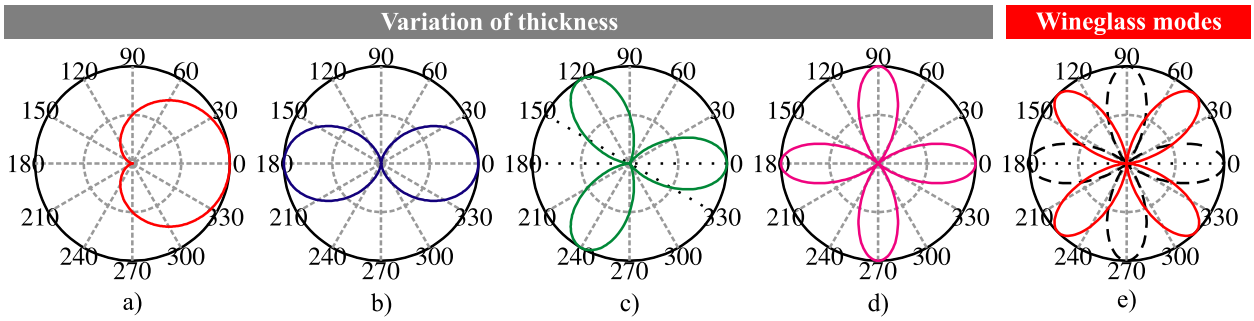


Fig. 3. Polar plots showing the first 4 thickness harmonics of thickness imperfections. Only the 4th thickness harmonic affects the frequency symmetry ($\Delta f$) of $n = 2$ wineglass modes. (a) 1st harmonic. (b) 2nd harmonic. (c) 3rd harmonic. (d) 4th harmonic. (e) $n = 2$ wineglass modes.

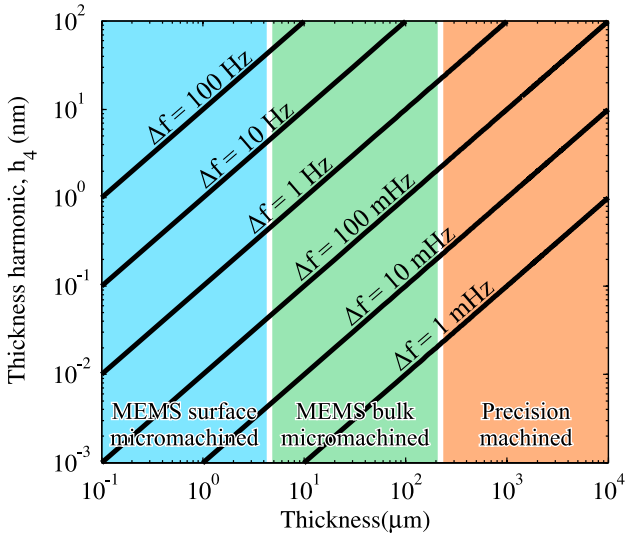


Fig. 4. Plot showing wineglass thickness vs thickness imperfections in the 4th harmonic and resulting frequency split. Going from precision machined wineglass resonators to micro-machined devices require 1 to 3 orders of magnitude improvement in fabrication tolerances due to the reduction in thickness.

shell mass and consequently the shell thickness [17], [18]:

$$\Delta f \cong f\frac{M_4}{M_0} \cong f\frac{h_4}{h_0}. \tag{3}$$

The equation 3 sets the basis for the scaling laws for frequency imperfections. Because of the thickness term in the denominator, the resonator will become more susceptible to frequency asymmetries as the thickness of the resonator decreases. This effect is shown in Fig. 4 for a 10 kHz resonator. The thickness axis is divided in 3 regimes from right to left: macro-scale devices such as the Hemispherical Resonator Gyroscopes [1], bulk micro-machined devices which have a thickness range of 10 $\mu$m to 250 $\mu$m and surface micro-machined wineglass resonators which have a thickness range of 100 nm to 10 $\mu$m. As can be seen in Fig. 4 going from macro-scale devices to MEMS wineglass resonators requires 1 to 3 orders of magnitude improvement in absolute tolerances to obtain the same frequency symmetry ($\Delta f$).

### *B. Stability of Micro-Glassblown Structures*

During micro-glassblowing, surface tension forces become active for a brief duration. These forces work towards minimizing the surface energy of the resonator and as a result mitigate the effects of imperfections, such as surface roughness or structural asymmetry. However, if care is not taken, surface tension forces can work towards unbalancing the resonator by creating a pressure instability within the micro-glassblown inverted-wineglass structure.

To analyze this effect we start with the Young–Laplace equation for surface tension:

$$\Delta P = 2\,\gamma\,(\frac{1}{R_1} + \frac{1}{R_2}), \tag{4}$$

where $\Delta P$ is the pressure, $\gamma$ is the surface tension coefficient, $R_1$ and $R_2$ are the principal radii of curvature of an arbitrary surface. The coefficient 2 on the right hand side comes from the fact that the micro-glassblown structures have two interface surfaces (inner and outer surfaces), as opposed to a single interface surface such as a droplet of water.

The curvature of an inverted-wineglass structure can be approximated as a hemi-toroid where the principal radius of curvature becomes the major and the minor radius of the hemi-toroid ($R_1 = R$ and $R_2 = r$ respectively). And the minor radius of the hemi-toroid will depend on the height ($l$) of the structure according to the following geometric expression:

$$r = \frac{l^2 + r_0^2}{2l}, \tag{5}$$

where $r_0$ is the half-width of the trench opening.

Equation 4 and 5 can be combined to solve for surface tension induced pressure difference with respect to $l$. Figure 5 shows results of this calculation for inverted-wineglass structures with $R = 1$ mm and $r_0 = 100\,\mu$m to $1600\,\mu$m.

It can be seen that $\Delta P$ has a local maxima for all designs, which occur at $r_0 = l$. Interpretation of this result is that the surface tension forces will progressively increase and work towards keeping the structure symmetric if the structure is designed to have $l < r_0$. However, if the shell is glass-blown beyond $l > r_0$, the surface tension forces will progressively decrease. As a result any perturbation on the geometric shape will be amplified by the further reduction in surface tension induced pressure $\Delta P$, creating an unstability within the micro-glassblown structure.

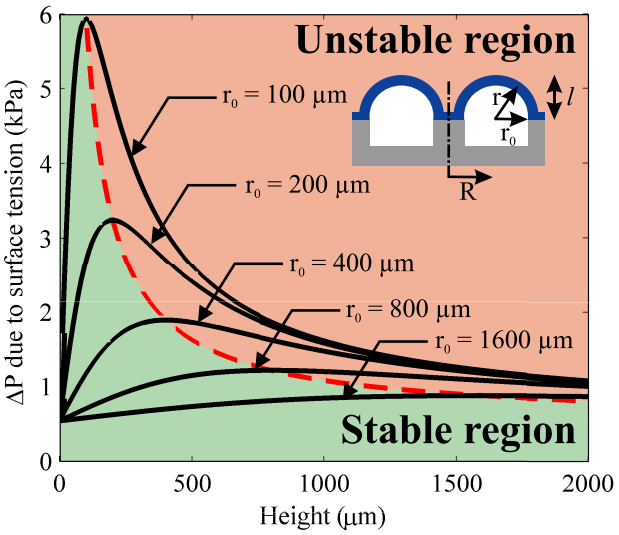


Fig. 5. Surface tension induced pressure differential depends on geometric parameters such as cavity radius ($r_0$) and height ($l$)). $l = r_0$ marks the critical Stable region for micro-glassblowing of inverted wineglass structures.

To summarize, in order to achieve high structural symmetry and avoid surface tension induced instability during micro-glassblowing, inverted-wineglass structures should be designed to have $l < r_0$.

### C. Factors Affecting Frequency Symmetry

Fabrication process was optimized with two design goals in mind: (1) batch-scale compatible fabrication process, (2) elimination of process steps that can contribute to frequency asymmetry. For compatibility with batch-scale fabrication, only standard MEMS processes were used in fabrication of the micro-wineglass resonators: the process consists of two lithography steps, three dry etch steps, one electroplating and one sputtering step. The glassblowing is performed in a standard rapid thermal annealing system, which can provide uniform heating and cooling for up to 6″ diameter wafers (Heatpulse 610 RTA).

It has been found that edge defects and thermal/mechanical perturbations during glassblowing are the primary factors affecting the frequency symmetry of micro-glassblown resonators, Table I. These effects were eliminated by using an improved dry-etch mask [19] and optimizing the glassblowing conditions to have uniform temperature and gas flow. In order to minimize the frequency asymmetry further, additional precautions were taken. Pick-and-place or wafer alignment steps that can create misalignment and potentially contribute to frequency asymmetry were eliminated. Contribution of mask misalignment errors were also minimized by incorporating only two lithography steps and using a self-aligned stem structure. Both of the lithography steps were performed before the micro-glassblowing step, while the device layer is still two dimensional, Fig. 6(b). This eliminates the need for more challenging patterning techniques such as 3-D lithography, shadow masks or laser ablation of the 3-D structure. Finally, anisotropic dry etching was used to define both the substrate cavity and the outer perimeter of the structure, eliminating etch asymmetries that may occur due to crystalline orientation of silicon [5].

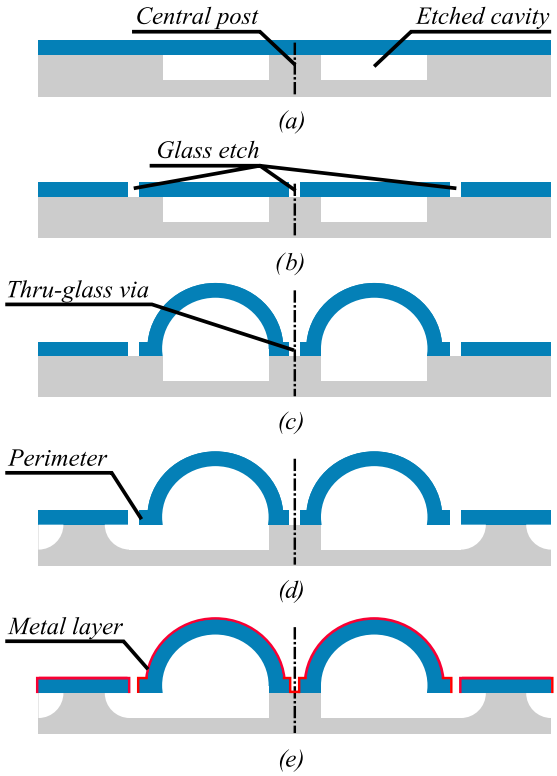


Fig. 6. Process flow for fabricating micro-glassblown wineglass resonators with integrated electrodes. (a) Silicon subsrate is etched and glass device layer is bonded. (b) Glass layer is etched, defining the perimeter and electrodes. (c) Wafer stack is glassblown creating the 3-D shell structure. (d) Silicon is etched using $XeF_2$ to release the wineglass structure. (e) A thin metal layer is blanket coated using sputtering.

## III. Fabrication

In order to fabricate the micro-wineglass resonators, first cylindrical cavities with a central post were etched to 250 $\mu$m depth on a 4″ silicon substrate wafer using DRIE, Fig. 6(a). Then, a thin glass layer (100 $\mu$m) was anodically bonded onto the silicon substrate. Anodic bonding was performed using a DC voltage of 600 V and a load of 100 N at 400 °C. The glass layer was bonded to the substrate along the perimeter of the cylindrical cavity and at the central post, hermetically sealing atmospheric pressure air within the cavities. This was followed by deep glass dry etching to define the outer perimeter of the wineglass resonator and central via hole, Fig. 6(b). Capacitive gaps and individual electrodes as well as the central via hole were defined at this step. The glass etching was performed using a magnetic neutral loop discharge plasma oxide etcher (ULVAC NLD 570 Oxide Etcher) [19]. A ~5 $\mu$m thick low-stress electroplated Cr/Ni hard-mask was used to etch the 100 $\mu$m deep trenches. This was followed by micro-glassblowing of the wafer stack at 875 °C inside a RTA system, where the glass layer becomes viscous and the air inside the cavity expands, creating the 3-D shell structure, Fig. 6(c).

TABLE I
SUMMARY OF FABRICATION DEFECTS AND REDUCTION APPROACH

| Cause | Defect | Reduction Approach |
|---|---|---|
| **Dry etch defects** | Micro-masking & mouse bites | Improved dry-etch mask |
| **Perturbations at High Temp.** | Structural deformation | Uniform temp. / gas flow |
| **Mask Misalignment** | $< 2\mu$m misalignment | Stepper |
| **Wafer flatness** | $< 0.1^\circ$ across wafer | Ultra-flat wafers |
| **Wafer bow** | $< 0.1^\circ$ across wafer | CTE matched materials |

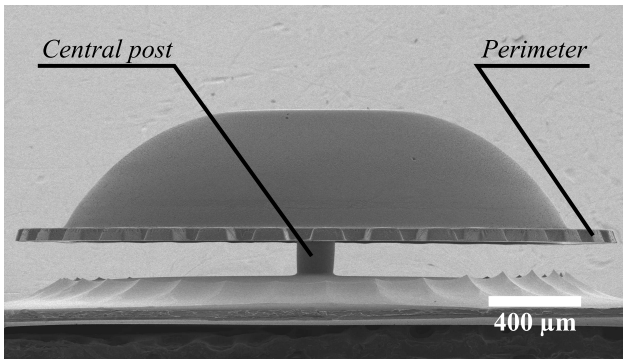


Fig. 7. SEM image of a stand-alone micro-wineglass structure after release. Diameter 4.4 mm, thickness 50 $\mu$m.

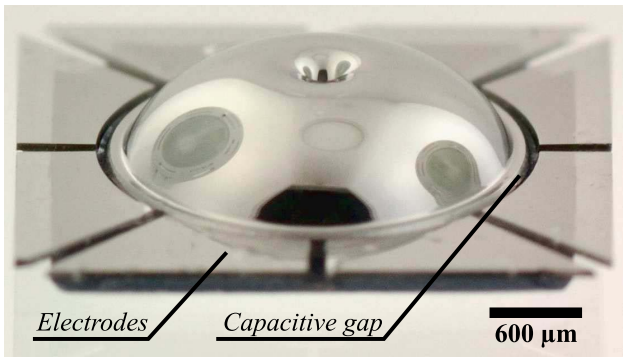


Fig. 8. Metallized micro-wineglass structure with integrated electrodes. Diameter 4.4 mm, thickness 50 $\mu$m.

Once the 3-D micro-glassblown structure forms, the wafer was rapidly cooled to room temperature for solidification. During the micro-glassblowing step, the perimeter of the wineglass structure and the planar electrodes do not deform as there is no etched cavity under these structures, enabling lithographic definition of the capacitive gaps. The next step was $XeF_2$ etching of the substrate underneath the glass layer in order to release the wineglass resonator along its perimeter, Fig. 6(d). $XeF_2$ was chosen because of the extremely high glass to silicon selectivity (as high as 1:1000 selectivity). Once the etch was complete a free standing micro-wineglass structure with a self-aligned stem structure was obtained, Fig 7.

Final step of the fabrication process is blanket metallization by sputtering, Fig. 8. A 30 nm sputtered Iridium layer was chosen for the metal layer, because of high conductivity, corrosion resistance and the ability to apply without utilizing an adhesion layer (such as Cr or Ti). The metal layer coats the top surface of the resonator shell, the side walls of the

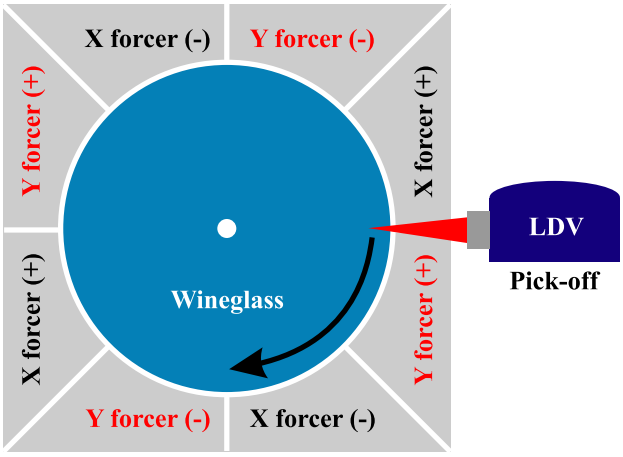


Fig. 9. Laser Doppler Vibrometer was used to scan along the perimeter of the wineglass to map the mode shapes associated with X forcer and Y forcer electrodes.

capacitive gaps as well as inside of the central via hole. However, directionality of the sputtering process prevents the metal layer from coating the undercut created by the $XeF_2$ etch, electrically isolating the electrodes and the resonator, Fig. 6(e). Electrical feed-through to the resonator was obtained through the central via structure, which connects the resonator to the substrate.

## IV. TESTING AND CHARACTERIZATION

In order to experimentally identify the mode shapes associated with different resonant frequencies, the wineglass resonator was excited electrostatically using the integrated electrode structures. The amplitude of motion at different points along the outer perimeter was mapped using laser Doppler vibrometry, creating a representation of the mode-shapes associated with different resonant frequencies, Fig. 9. This was accomplished by moving the laser spot along the perimeter while driving the resonator with two different sets of electrode configurations for each degenerate wineglass mode, Fig. 10. For n = 2 wineglass mode, 4 electrodes were used for each degenerate mode with 45° angle between the two electrode sets. Two of the electrodes were driven in anti-phase, this electrode configuration excites the n = 2 wineglass mode selectively, while suppressing all other modes. For n = 3 mode, a single electrode was used for each degenerate wineglass mode. Excitation using a single electrode was necessary, as a balanced excitation using 2 or 4 electrodes inherently suppresses the n = 3 mode. A DC bias voltage

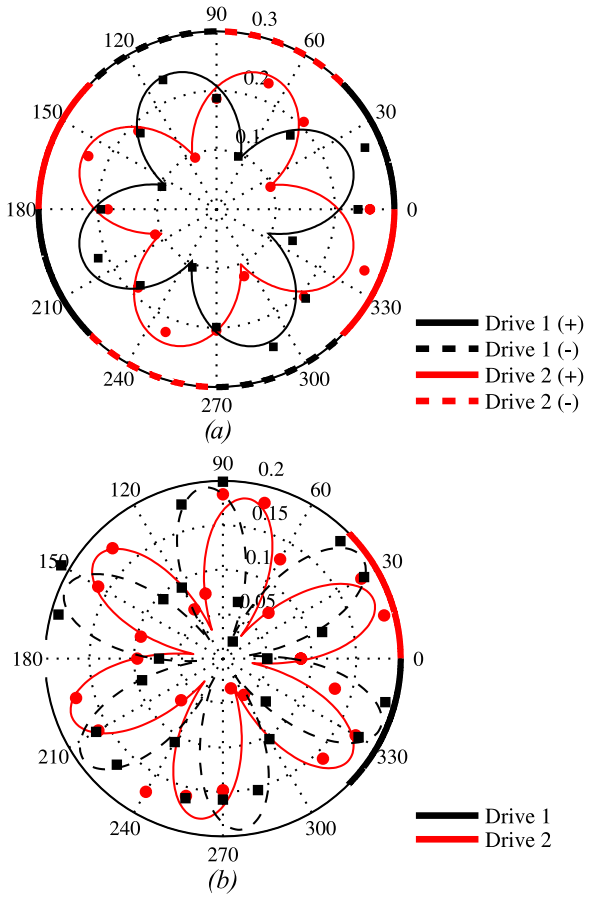


Fig. 10. Measured velocity amplitude distribution (mm/s) identifying. (a) n = 2 and (b) n = 3 wineglass modes.

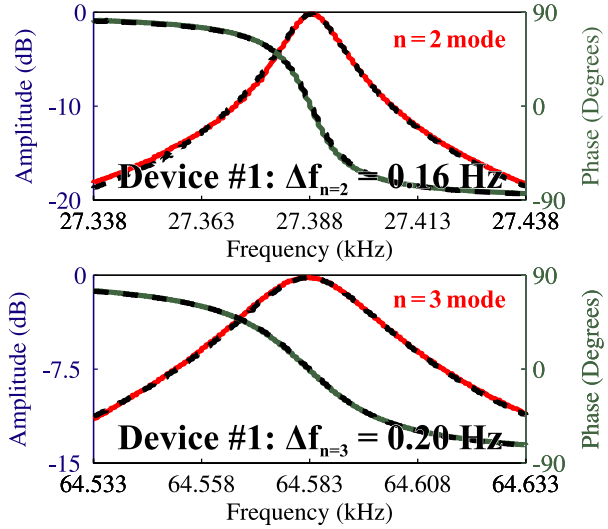


Fig. 11. Experimental frequency sweeps of n = 2 and n = 3 wineglass modes, showing $\Delta f = 0.16$ Hz and $\Delta f = 0.20$ Hz, respectively.

of 100 V and an AC drive voltage of 5 V was used in all experiments ($V_{DC}$ = 100 V and $V_{AC}$ = 5 V). Large drive voltages used in this experiment were due to large capacitive gaps of the current prototypes ($> 30\ \mu$m).

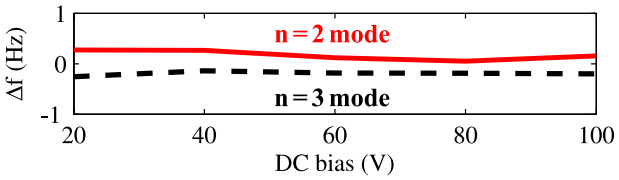


Fig. 12. Frequency split vs DC bias, showing that the frequency split is within 1 Hz independent of DC bias (DC bias was varied between 20–100 V with 20 V increments).

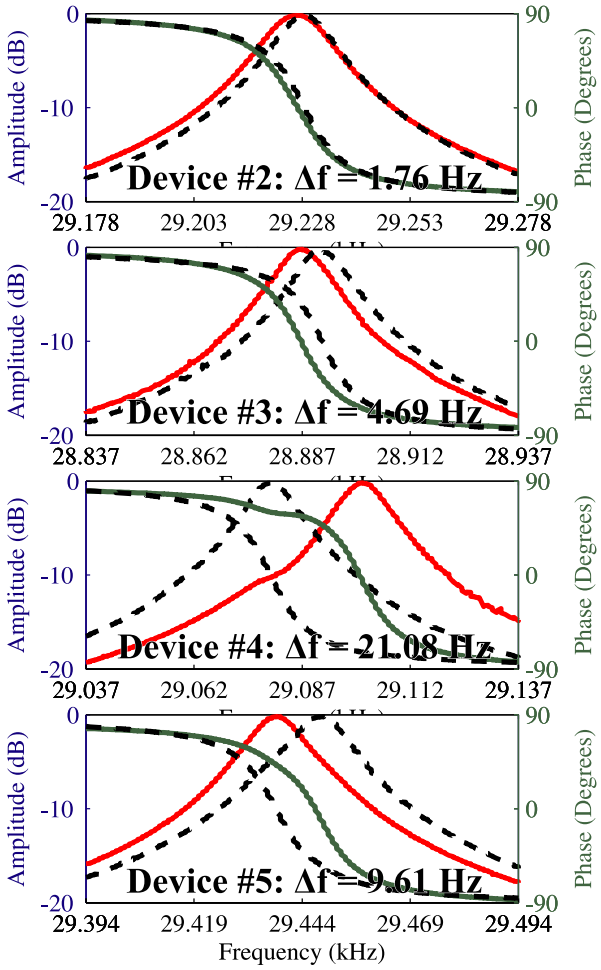


Fig. 13. Frequency sweeps of n = 2 mode of 4 additional wineglass resonators, showing f values in the range of 1.76 Hz to 21.08 Hz.

For device #1, center frequencies of degenerate wineglass modes were identified at 27389 Hz and 64583 Hz for n = 2 and n = 3 wineglass modes, respectively, Fig. 11. Frequency splits between the two degenerate modes were measured by fitting a second order system response onto the frequency sweep data of each degenerate wineglass mode. For the device #1 highlighted in these measurements, frequency split ($\Delta$f) of 0.15 Hz and 0.2 Hz were observed for n = 2 and n = 3 wineglass modes with 95% confidence levels at 0.23 Hz for n = 2 and 0.3 Hz for n = 3, Fig. 11. In order to estimate the contribution of electrostatic spring softening effect, DC bias

TABLE II
TABLE SUMMARIZING FREQUENCY SPLITS AND CENTER FREQUENCY OF 5 DIFFERENT MICRO-WINEGLASS STRUCTURES

| Device # | Center Freq. (Hz) | $\Delta f$ (Hz) | $\sigma$ (Hz) | $\Delta f/f$ (ppm) |
|---|---|---|---|---|
| 1 | 27388.65 | 0.16 | 0.04 | 5.67 |
| 2 | 28889.18 | 4.69 | 0.05 | 162.18 |
| 3 | 29227.60 | 1.76 | 0.05 | 60.30 |
| 4 | 29090.38 | 21.08 | 0.06 | 724.65 |
| 5 | 29442.98 | 9.61 | 0.07 | 326.40 |

voltage was varied between 20 V–100 V, frequency split stayed below 1 Hz for both modes, attributing the low frequency split to high structural symmetry and not to capacitive tuning, Fig. 12.

In order to verify the repeatability of the results, four other wineglass resonators were characterized using the same method described above. Three of the five wineglass resonators had frequency split less than 5 Hz, one less than 10 Hz for the n = 2 wineglass mode, with one outlier at $\Delta f \approx 21$ Hz, Fig. 13.

## V. CONCLUSION

Micro-glassblown resonators with integrated electrode structures were fabricated. Electrostatic excitation of micro-glassblown resonators using integrated electrode structures were experimentally demonstrated for the first time. Integrated electrode structures within the glass device layer eliminate the need for additional assembly steps and misalignment errors between the resonator and the electrodes. In addition, by using the same material for the resonator and the electrodes, thermal stress effects due to thermal expansion mismatch are reduced.

Identification of the mode shapes using laser Doppler vibrometry revealed frequency splits as low as $< 1$ Hz at $\sim 27$ kHz center frequency on device #1, giving a relative frequency split of $\Delta f_{n=2}/f_{n=2} < 10$ ppm (or 0.001 %). Three of the five wineglass resonators had frequency split less than 5 Hz, one less than 10 Hz for the n = 2 wineglass mode, with one outlier at $\Delta f \approx 21$ Hz, Table II.

The focus of this study was on frequency symmetry of micro-glassblown resonators, for this reason borosilicate glass was used as the resonator material. As expected, low Q-factors (several thousands) were observed due to the high internal dissipation of borosilicate glass. Also, large capacitive gaps were used for electrostatic transduction, due to challenges associated with deep glass dry etching, which required use of high DC bias voltages for excitation. Future research directions include high-Q materials such as ULE TSG / fused silica for the resonator material as well as smaller capacitive gaps in order to achieve high performance rate-integrating gyroscope operation. ULE TSG / fused silica glassblowing process previously demonstrated by the authors [12], [13] and a high temperature substrate such as tungsten may help achieve the Q-factors required for rate-integrating gyroscope operation. Improved dry etching performance of 7:1 aspect ratio also demonstrated by the authors [19], coupled with a thinner device layer is expected to provide smaller capacitive gaps and improved electrostatic transduction.

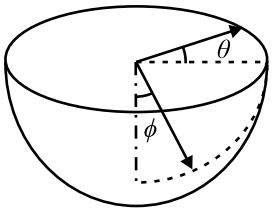


Fig. 14. Sketch of an ideal wineglass (perfectly spherical), showing $\theta$ as the angle along the central axis of symmetry and, $\phi$ as the secondary angle.

These results demonstrate the feasibility of surface tension driven micro-glassblowing process as a means to fabricate extremely symmetric and smooth 3-D wineglass resonators. High structural symmetry ($\Delta f < 1$ Hz) and atomically smooth surfaces (0.23 nm Sa) of the resonators may enable new classes of high performance 3-D MEMS devices, such as rate-integrating MEMS gyroscopes and mode-matched angular rate gyroscopes.

## APPENDIX

To understand why only the 4th harmonic of the thickness variation has an effect on fundamental frequency splitting ($\Delta f$), we look at the vibrational kinetic energy of the resonator, which is used in Rayleigh-Ritz solution of the resonance frequencies of wineglass geometries [20], [21]:

$$K_0 = \frac{1}{2} r\rho h \int_0^{\pi/2} \int_0^{2\pi} (\dot{u}^2 + \dot{v}^2 + \dot{w}^2) \sin\phi d\theta d\phi, \quad (6)$$

where $\dot{u}, \dot{v}$ and $\dot{w}$ are the velocity terms, which are represented as:

$$u = U(\phi, t)\ \sin(n\theta), \quad (7)$$

$$v = V(\phi, t)\ \sin(n\theta), \quad (8)$$

$$w = W(\phi, t)\ \sin(n\theta), \quad (9)$$

and $r$ is the radius of an ideal wineglass $\rho$ is the density of the material, $\theta$ is the angle along the central axis of symmetry and, $\phi$ is the secondary angle, Fig. 14.

However, above equations for vibrational kinetic energy assume a perfectly symmetric geometry with no thickness variation. If we derive the same equation for an imperfect wineglass resonator with a thickness variation as in equation 1, then the kinetic energy equation will become:

$$K = \frac{1}{2} r\rho \int_0^{\pi/2} \int_0^{2\pi} (\dot{u}^2 + \dot{v}^2 + \dot{w}^2)\, h(\varphi)\ \sin\phi d\theta d\phi. \quad (10)$$

The difference between kinetic energies of the ideal wineglass resonator in equation 6 and the one with thickness variations in equation 10 can be summarized as:

$$K = K_0 + K_{unbalance}. \quad (11)$$

The $K_{unbalance}$ term, which is the difference in kinetic energy due to thickness variations becomes:

$$K_{unbalance} = \frac{1}{2} r\rho \int_0^{\pi/2} \int_0^{2\pi} A\ B\ \sin\phi d\theta d\phi, \quad (12)$$

where $A$ is a collection of velocity terms and:

$$B = h_i \sin(2n\theta) \sin(i\theta). \quad (13)$$

Index $i$ is the thickness harmonics under consideration. The $B$ term is the focus of the analysis, as it will make the whole integral (and consequently $K_{unbalance}$) equal to zero if $2n \neq i$. In other words, only thickness variations with harmonics at $2n = i$ can cause changes in the kinetic energy (and frequency) of the wineglass.

## ACKNOWLEDGMENT

This material is based upon work supported by DARPA grant W31P4Q-11-1-0006 (Program Manager Dr. William Chappell). Devices were designed and tested in UCI Micro-Systems Lab. Authors would like to thank UCI INRF staff Jake Hes, Mo Kebaili, Vu Phan and Lifeng Zheng for their help and valuable suggestions on the fabrication aspects of the project.

## REFERENCES

[1] D. M. Rozelle, "The hemispherical resonator gyro: From wineglass to the planets," in *Proc. AAS/AIAA Space Flight Mech. Meeting*, 2009, pp. 1157–1178.

[2] C. C. Painter and A. M. Shkel, "Active structural error suppression in MEMS vibratory rate integrating gyroscopes," *IEEE Sensors J.*, vol. 3, no. 5, pp. 595–606, Oct. 2003.

[3] L. D. Sorenson, P. Shao, and F. Ayazi, "Effect of thickness anisotropy on degenerate modes in oxide micro-hemispherical shell resonators," in *Proc. IEEE MEMS*, Taiwan, Jan. 2013, pp. 169–172.

[4] M. L. Chan, J. Xie, P. Fonda, H. Najar, K. Yamazaki, L. Lin, *et al.*, "Micromachined polycrystalline diamond hemispherical shell resonators," in *Proc. Solid-State Sensors, Actuat., Microsyst. Workshop*, 2012, pp. 355–358.

[5] L. C. Fegely, D. N. Hutchison, and S. A. Bhave, "Isotropic etching of 111 SCS for wafer-scale manufacturing of perfectly hemispherical silicon molds," in *Proc. Solid-State Sensors, Actuat., Microsyst. Workshop*, Beijing, China, Jun. 2011, pp. 2295–2298.

[6] Y. Xie, H. C. Hsieh, P. Pai, H. Kim, M. Tabib-Azar, and C. H. Mastrangelo, "Precision curved micro hemispherical resonator shells fabricated by poached-egg micro-molding," in *Proc. IEEE Sensors*, Oct. 2012, pp. 1–4.

[7] B. Sarac, G. Kumar, T. Hodges, S. Ding, A. Desai, and J. Schroers, "Three-dimensional shell fabrication using blow molding of bulk metallic glass," *J. Microelectromech. Syst.*, vol. 20, no. 1, pp. 28–36, 2011.

[8] J. Cho, J. Yan, J. A. Gregory, H. Eberhart, R. L. Peterson, and K. Najafi, "High-Q fused silica birdbath and hemispherical 3-D resonators made by blow torch molding," in *Proc. IEEE MEMS*, Taipei, Taiwan, Jan. 2013, pp. 177–180.

[9] I. P. Prikhodko, S. A. Zotov, A. A. Trusov, and A. M. Shkel, "Microscale glass-blown three-dimensional spherical shell resonators," *J. Microelectromech. Syst.*, vol. 20, no. 3, pp. 691–701, Jun. 2011.

[10] E. J. Eklund and A. M. Shkel, "Glass blowing on a wafer level," *J. Microelectromech. Syst.*, vol. 16, no. 2, pp. 232–239, Apr. 2007.

[11] S. A. Zotov, I. P. Prikhodko, A. A. Trusov, and A. M. Shkel, "3-D micromachined spherical shell resonators with integrated electromagnetic and electrostatic transducers," in *Proc. Solid-State Sensors, Actuat., Microsyst. Workshop*, 2010, pp. 11–14.

[12] D. Senkal, C. R. Raum, A. A. Trusov, and A. M. Shkel, "Titania silicate/fused quartz glassblowing for 3-D fabrication of low internal loss wineglass micro-structures," in *Proc. Solid-State Sensors, Actuat., Microsyst. Workshop*, 2012, pp. 267–270.

[13] D. Senkal, M. J. Ahamed, A. A. Trusov, and A. M. Shkel, "High temperature micro-glassblowing process demonstrated on fused quartz and ULE TSG," *Sens. Actuators A, Phys.*, vol. 201, pp. 525–531, Oct. 2013.

[14] D. Senkal, M. J. Ahamed, A. A. Trusov, and A. M. Shkel, "Adaptable test-bed for characterization of micro-wineglass resonators," in *Proc. IEEE MEMS*, Taipei, Taiwan, Jan. 2013, pp. 469–472.

[15] D. Senkal, M. J. Ahamed, A. A. Trusov, and A. M. Shkel, "Demonstration of sub-Hz frequency symmetry in micro-glassblown wineglass resonators with integrated electrodes," in *Proc. Solid-State Sensors, Actuat. Microsyst. Conf.*, Barcelona, Spain, 2013, pp. 1380–1383.

[16] B. S. Lunin, *Physical and Chemical Bases for the Development of Hemispherical Resonators for Solid-State Gyroscopes*. Moscow, Russia: Moscow Aviation Institute, 2005.

[17] V. F. Zhuravlev and D. M. Klimov, *A Hemispherical Resonator Gyroscope*. Moscow, Russia: Nauka, 1985.

[18] N. E. Egarmin and V. E. Yurin, *Introduction to Theory of Vibratory Gyroscopes*. Moscow, Russia: Binom, 1993.

[19] M. J. Ahamed, D. Senkal, A. A. Trusov, and A. M. Shkel, "Deep NLD plasma etching of fused silica and borosilicate glass," in *Proc. IEEE Sensors*, Baltimore, MD, USA, Nov. 2013.

[20] S. Choi and J. H. Kim, "Natural frequency split estimation for inextensional vibration of imperfect hemispherical shell," *J. Sound Vib.*, vol. 330, no. 9, pp. 2094–2106, Apr. 2011.

[21] S. Y. Choi, Y. H. Na, and J. H. Kim, "Thermoelastic damping of inextensional hemispherical shell," in *Proc. World Acad. Sci., Eng. Technol.*, 2009, pp. 198–203.

**Doruk Senkal** (S'13) received B.S. degree in mechanical engineering from Middle East Technical University, Ankara, Turkey in 2007 and the M.S. degree in mechanical engineering from Washington State University, Vancouver, in 2009. He is currently a graduate student research assistant at the University of California, Irvine Microsystems Laboratory, working toward a Ph.D. in mechanical engineering with a focus on microelectromechanical systems. His research interests include design and control of degenerate mode gyroscopes, 3-D MEMS resonators, MEMS bulk micro-machining and micro-glassblowing.

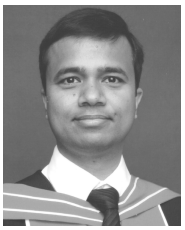

**Mohammed J. Ahamed** (M'13) received the M.A.Sc. and Ph.D. degrees in Mechanical Engineering from the University of Toronto, Toronto, ON, Canada, in 2006 and 2011 respectively. He is currently a Post-doctoral Fellow at the University of California, Irvine, where he is developing 3-D micro-hemispherical resonators. His research interests include MEMS resonators, sensors, actuators, microfluidics and biomedical lab-on-a-chip technology.

**Alexander A. Trusov** (M'06) Ph.D. is a Senior Research Scientist with Northrop Grumman Corporation, where he focuses on R&D of advanced navigation sensors and instruments. Dr. Trusov received the B.S. and M.S. degrees in applied mathematics and mechanics from Moscow State University, Moscow, Russia, in 2004, and the M.S. and Ph.D. degrees in mechanical and aerospace engineering from the University of California, Irvine (UCI), CA, USA, in 2006 and 2009, respectively. From 2009 to 2013, he was a Project Scientist in the Mechanical and Aerospace Department at UCI, where he served as the PI and a co-PI on more than half a dozen of DoD sponsored projects. Dr. Trusov's research interests include design, modeling, fabrication, and vacuum packaging of micromachined inertial systems, sensor and instrument self-calibration, design of characterization experiments, and statistical data processing and analysis. Dr. Trusov has published over 60 journal and conference papers and has 5 issued U.S. patents (half a dozen more pending) on these topics. He was a recipient of the Outstanding Paper Award at Transducers 2011, the Design Contest Award at the System-on-Chip Conference 2011, and the Best Paper Award at the IMAPS Device Packaging Conference 2012. Dr. Trusov currently serves on program committees for the Saint Petersburg International Conference on Integrated Navigation Systems, the IEEE International Symposium on Inertial Sensors and Systems, and the IEEE/ION Position Location and Navigation Symposium. He is a member of the ASME, IEEE, and ION.

**Andrei M. Shkel** (S'95–A'98–SM'08) received the diploma degree (with excellence) in mechanics and mathematics from Moscow State University, Russia, in 1991, and the Ph.D. degree in mechanical engineering from the University of Wisconsin, Madison, USA, in 1997. In 2000, he joined the faculty of the University of California, Irvine, where is currently a Professor in the Department of Mechanical and Aerospace Engineering, with a joint appointment to the Department of Electrical Engineering and Computer Science and the Department of Biomedical Engineering.

From 2009 to 2013, Dr. Shkel served as a Program Manager in the Microsystems Technology Office of the Defense Advanced Research Projects Agency (DARPA), Arlington, VA, where he created and managed a comprehensive portfolio of programs focused on microtechnology for Positioning, Navigation, and Timing (PNT) applications, including the nationwide programs Micro Rate Integrating Gyroscope (MRIG), Primary and Secondary Calibration on Active Layer (PASCAL), Timing and Inertial Measurement Unit (TIMU), and Chip-Scale Combinatorial Atomic Navigator (C-SCAN). His professional interests, reflected in over 170 publications and two books, include solid-state sensors and actuators, MEMS-based neuroprosthetics, sensor-based intelligence, and control theory. He holds 24 U.S. and worldwide patents (12 are pending) on micromachined angle-measuring gyroscopes, wide-bandwidth rate gyroscopes, design and fabrication of light manipulators and tunable optical filters, and hybrid micromachining processes. His current interests center on the design, manufacturing, and advanced control of micro-electro-mechanical systems (MEMS) for biomedical and inertial navigation applications, in particular, on the development of high-precision micromachined gyroscopes. Dr. Shkel has served on a number of editorial boards, most recently as Editor of the JOURNAL OF MICROELECTROMECHANICAL SYSTEMS, Editorial Board Member for the *International Journal on Smart Structures and Systems*, TPC Member of Hilton Head 2009, and General Chair of 2005 IEEE Sensors Conference. He has been awarded the IEEE Sensors Council 2009 Technical Achievement Award, 2005 NSF CAREER Award, the 2002 George E. Brown, Jr. Award, and the 2006 Best Faculty Research Award.

In 2013, he received the Office of the Secretary of Defense Medal for Exceptional Public Service for his work at DARPA as a Program Manager.